

# Ring closure activates yeast $\gamma$ TuRC for species-specific microtubule nucleation

Justin M Kollman<sup>1</sup>, Charles H Greenberg<sup>2-4</sup>, Sam Li<sup>5</sup>, Michelle Moritz<sup>5</sup>, Alex Zelter<sup>1</sup>, Kimberly K Fong<sup>1</sup>, Jose-Jesus Fernandez<sup>6</sup>, Andrej Sali<sup>2-4</sup>, John Kilmartin<sup>7</sup>, Trisha N Davis<sup>1</sup> & David A Agard<sup>5,8</sup>

The  $\gamma$ -tubulin ring complex ( $\gamma$ TuRC) is the primary microtubule nucleator in cells.  $\gamma$ TuRC is assembled from repeating  $\gamma$ -tubulin small complex ( $\gamma$ TuSC) subunits and is thought to function as a template by presenting a  $\gamma$ -tubulin ring that mimics microtubule geometry. However, a previous yeast  $\gamma$ TuRC structure showed  $\gamma$ TuSC in an open conformation that prevents matching to microtubule symmetry. By contrast, we show here that  $\gamma$ -tubulin complexes are in a closed conformation when attached to microtubules. To confirm the functional importance of the closed  $\gamma$ TuSC ring, we trapped the closed state and determined its structure, showing that the  $\gamma$ -tubulin ring precisely matches microtubule symmetry and providing detailed insight into  $\gamma$ TuRC architecture. Importantly, the closed state is a stronger nucleator, thus suggesting that this conformational switch may allosterically control  $\gamma$ TuRC activity. Finally, we demonstrate that  $\gamma$ TuRCs have a strong preference for tubulin from the same species.

Microtubule nucleation is mediated *in vivo* by  $\gamma$ -tubulin complexes, which allow cells to control both the location and timing of new microtubule growth. The conserved core of the nucleating machinery is the  $\gamma$ TuSC, a 300-kDa V-shaped structure with two copies of  $\gamma$ -tubulin and one copy each of the accessory proteins GCP2 and GCP3, which are distant homologs of each other. GCP2 and GCP3 form the elongated arms of the complex, with  $\gamma$ -tubulin at each tip of the V<sup>1,2</sup>. Low-resolution structural studies of isolated  $\gamma$ TuSCs previously showed that the complex is flexible, with a hinge-like motion near the center of the GCP3 arm<sup>2</sup>. In most eukaryotes, several other accessory proteins, GCP4–GCP6, assemble with multiple  $\gamma$ TuSCs to form the  $\gamma$ TuRC<sup>3,4</sup>.  $\gamma$ TuRC has long been thought to function as a template, presenting a ring of  $\gamma$ -tubulins from which microtubules grow<sup>3-7</sup>.

*Saccharomyces cerevisiae* lacks the  $\gamma$ TuRC-specific accessory proteins found in other eukaryotes, and it nucleates microtubules from  $\gamma$ TuSC oligomers. These oligomers are anchored to the nuclear face of the spindle pole body by the coiled-coil protein Spc110 (refs. 8,9). Isolated  $\gamma$ TuSCs have a weak propensity to self-assemble, and the N-terminal domain of Spc110 (Spc110<sub>1-220</sub>) stabilizes these interactions to promote the formation of extended spiral-shaped oligomers that have 13  $\gamma$ -tubulins per turn<sup>10</sup>, a number matching the protofilament number of *in vivo* microtubules<sup>11</sup>. Extended  $\gamma$ TuSC polymers have not been observed at spindle pole bodies<sup>12</sup>, and although some estimates of the subunit number have been made<sup>13</sup>, the overall size and organization of the functional  $\gamma$ TuSC oligomer *in vivo* is unclear.

Although the nucleation activity of yeast  $\gamma$ TuSC is entirely dependent on its oligomerization, unexpectedly the oligomers are configured

with microtubule-like  $\gamma$ -tubulin lateral contacts only between  $\gamma$ TuSCs, while within each  $\gamma$ TuSC the two  $\gamma$ -tubulins are held apart in an open conformation<sup>2,10</sup>. A consequence of the staggered lateral  $\gamma$ -tubulin interactions is a  $\gamma$ TuSC ring with a pitch  $\sim 25$  Å larger than that of microtubules (Supplementary Fig. 1). This conformation seems inconsistent with  $\gamma$ TuSC assemblies acting as efficient microtubule templates; indeed, microtubule nucleation experiments showed only a modest enhancement over background. Because of the flexibility observed within individual  $\gamma$ TuSCs<sup>2</sup>, however, we proposed that an allosterically regulated conformational change could result in a precise match to microtubule geometry, thus forming a template with increased nucleating activity<sup>5,10</sup>.

Here, we set out to determine the structure of the functional state of  $\gamma$ TuSC rings. We demonstrate that *in vivo* the minus ends of microtubules are anchored to the spindle pole body via a  $\gamma$ TuSC ring that is in a closed conformation and has a defined number of subunits. Although the *in vivo* drivers of ring closure are unknown, we could trap a closed state of  $\gamma$ TuSC oligomers by disulfide cross-linking, and we determined its structure at 6.9-Å resolution by cryo-EM. The closed state closely resembles the structure observed at minus ends, and conformational changes within each  $\gamma$ TuSC result in a nearly perfect match between the  $\gamma$ -tubulin ring and 13-protofilament-microtubule geometries. The closed state is more active than the open state, thus confirming that  $\gamma$ TuRC activity can be conformationally regulated. We also show that yeast  $\gamma$ TuSC is much more active with yeast tubulin than with vertebrate tubulin, demonstrating the importance of species specificity in nucleating activity. The high-resolution

<sup>1</sup>Department of Biochemistry, University of Washington, Seattle, Washington, USA. <sup>2</sup>Department of Bioengineering and Therapeutic Sciences, University of California at San Francisco, San Francisco, California, USA. <sup>3</sup>Department of Pharmaceutical Chemistry, University of California at San Francisco, San Francisco, California, USA. <sup>4</sup>California Institute for Quantitative Biosciences (QB3), University of California at San Francisco, San Francisco, California, USA. <sup>5</sup>Department of Biochemistry and Biophysics, University of California at San Francisco, San Francisco, California, USA. <sup>6</sup>Centro Nacional de Biotecnología, Consejo Superior de Investigaciones Científicas, Madrid, Spain. <sup>7</sup>Medical Research Council Laboratory of Molecular Biology, Cambridge, UK. <sup>8</sup>Howard Hughes Medical Institute, University of California at San Francisco, San Francisco, California, USA. Correspondence should be addressed to D.A.A. (agard@msg.ucsf.edu).

Received 23 July 2014; accepted 12 December 2014; published online 19 January 2015; doi:10.1038/nsmb.2953

structure of the closed state allowed us to generate a pseudoatomic model that provides a more detailed view of the interactions of components within the  $\gamma$ TuSC and of the nature of assembly contacts between  $\gamma$ TuSCs.

## RESULTS

### $\gamma$ TuSC binds microtubules in a closed conformation

A key question is whether or not  $\gamma$ TuSCs can actually form a structure that better matches microtubule symmetry. To answer this, we determined the conformational state of  $\gamma$ TuSC rings interacting with microtubules at the spindle pole. We examined the *in situ* structure of microtubule minus ends attached to the nuclear faces of purified spindle pole bodies by using cryo-electron tomography (Fig. 1a). We averaged 1,156 individual capped microtubule minus ends to generate a structure at 38-Å resolution (0.5 Fourier shell correlation (FSC) cutoff criterion). The structure reveals an asymmetric cap in which individual  $\gamma$ TuSC subunits can be discerned in most directions. The  $\gamma$ TuSCs form a lock washer-shaped spiral that rises 120 Å (Fig. 1b and Supplementary Movie 1), a value similar to the pitch of 13-protofilament microtubules<sup>14</sup>. This pitch is in contrast to the 147-Å pitch of reconstituted  $\gamma$ TuSC-Spc110<sub>1–220</sub> spirals<sup>10</sup>, thus indicating that when bound to microtubules *in vivo* the conformation of the  $\gamma$ TuSC ring is different than that observed for our unbound rings *in vitro*<sup>2,10</sup>.

### Spc110 promotes formation of a defined yeast $\gamma$ TuRC

The structure of capped minus ends also reveals the number of  $\gamma$ TuSC oligomers *in vivo*. It has been assumed that functional  $\gamma$ TuSC oligomers would have six copies (with 12  $\gamma$ -tubulins and a gap at the 13th position) or seven copies (with an overlapping, inaccessible 14th  $\gamma$ -tubulin at the end) or would be variable in number<sup>6,15,16</sup>. In the minus-end structure, the last  $\gamma$ TuSC overlaps vertically with the first  $\gamma$ TuSC (Fig. 1b), thus indicating that the ring is formed from seven subunits. Unlike these defined seven-subunit rings, *in vitro* assembly of  $\gamma$ TuSC and Spc110<sub>1–220</sub> yields extended spirals<sup>10</sup>. However, we found that a longer Spc110 fragment (residues 1–401), with an additional 180 residues of predicted coiled coil, limited  $\gamma$ TuSC assemblies to single rings and smaller oligomers, thus suggesting that Spc110 sterically interferes with addition of more than seven  $\gamma$ TuSCs (Fig. 1c,d). Thus, Spc110 both promotes  $\gamma$ TuSC assembly and limits oligomer size, forming well-defined yeast  $\gamma$ TuRCs.

### $\gamma$ TuSC oligomers trapped in a closed state

Because  $\gamma$ TuSCs adopts a closed, microtubule-like geometry when interacting with microtubules, we sought to trap this closed state with engineered disulfide bonds to test the functional consequences of closure. Assuming that in a closed state  $\gamma$ -tubulin makes lateral contacts between the M and H1-S2 loops similar to those observed in the microtubule lattice<sup>14</sup> or  $\gamma$ -tubulin crystals<sup>17,18</sup> (Fig. 2a), we designed four sets of paired cysteine mutations: Asn57 Gly288; Ser58 Gly288; Asp128 Ser291; and Arg161 Arg341. We predicted the

sites to be juxtaposed at the inter- $\gamma$ TuSC assembly interface but widely separated at the intra- $\gamma$ TuSC interface (Fig. 2a). Thus, under oxidizing conditions a disulfide bond should readily form between  $\gamma$ -tubulins from adjacent  $\gamma$ TuSCs but should form only between  $\gamma$ -tubulins within the same  $\gamma$ TuSC if that  $\gamma$ TuSC samples a closed state. We observed disulfide-bond formation only in the N57C G288C and S58C G288C mutants. Of the two, S58C G288C was better behaved in terms of oligomeric assembly, so we pursued structural and functional characterization of this complex, which we refer to as  $\gamma$ TuSC<sup>CC</sup>. The  $\gamma$ TuSC<sup>CC</sup> mutations, introduced into yeast on the only copy of  $\gamma$ -tubulin, did not affect viability or metaphase spindle organization (Supplementary Fig. 2). Thus, the mutations do not impair  $\gamma$ TuSC function in the context of the cell.

Under reducing conditions, individual  $\gamma$ TuSC<sup>CC</sup> had the same overall structure as the wild-type complex<sup>2</sup> (Supplementary Fig. 3a). Wild-type  $\gamma$ TuSC has a weak propensity to self-assemble into ring-like oligomers under a narrow range of salt concentrations (<200 mM KCl) and pH values (6.4–7.0). After removal of reducing reagents, however,  $\gamma$ TuSC<sup>CC</sup> spontaneously assembled into large oligomers at pH 7.6 and 500 mM KCl, conditions that strongly disfavor spontaneous assembly of wild-type  $\gamma$ TuSC (Supplementary Fig. 3b). This suggested that inter- $\gamma$ TuSC disulfide bonds stabilize weak interactions between  $\gamma$ TuSCs. SDS-PAGE of nonreduced  $\gamma$ TuSC<sup>CC</sup> revealed a ladder of cross-linked  $\gamma$ -tubulin oligomers, indicating that disulfide cross-links had formed both within and between  $\gamma$ TuSCs (Supplementary Fig. 3c). The presence of  $\gamma$ -tubulin oligomers with more than two chains means that both inter- and intra- $\gamma$ TuSC disulfide cross-links were formed, thus indicating trapping of a new conformation of  $\gamma$ TuSC that allowed formation of intra- $\gamma$ TuSC disulfide.

Next, we copurified the  $\gamma$ TuSC<sup>CC</sup>-Spc110<sub>1–220</sub> complex and observed that under reducing conditions it formed filaments similar to those in the wild-type complex. Under weakly oxidizing conditions, however, there were clearly two populations of filaments in the sample: one similar to the open wild-type filaments (Fig. 2b, blue arrows) and the other a new, more compact or closed form with a different helical pitch (Fig. 2b, orange arrows). The power spectrum of single filaments of the open form had a strong layer line at 147 Å, corresponding to the pitch of the wild-type filament, whereas the closed form had a layer line at 122 Å, very close to the pitch of a 13-protofilament microtubule (Fig. 2c). Single filaments appeared to be predominantly

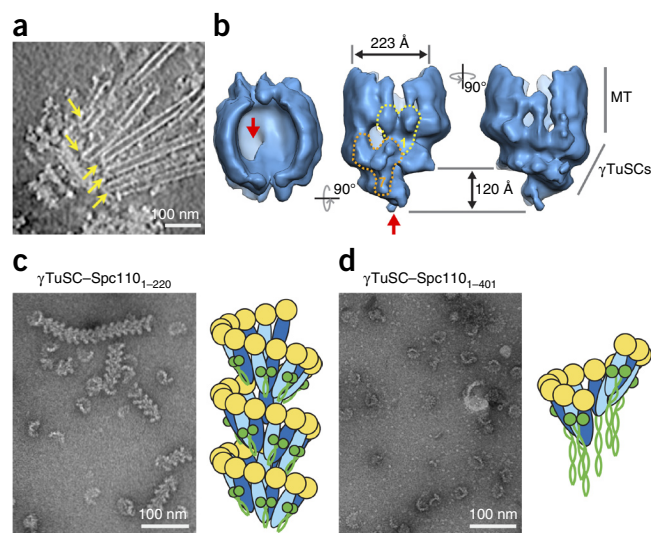
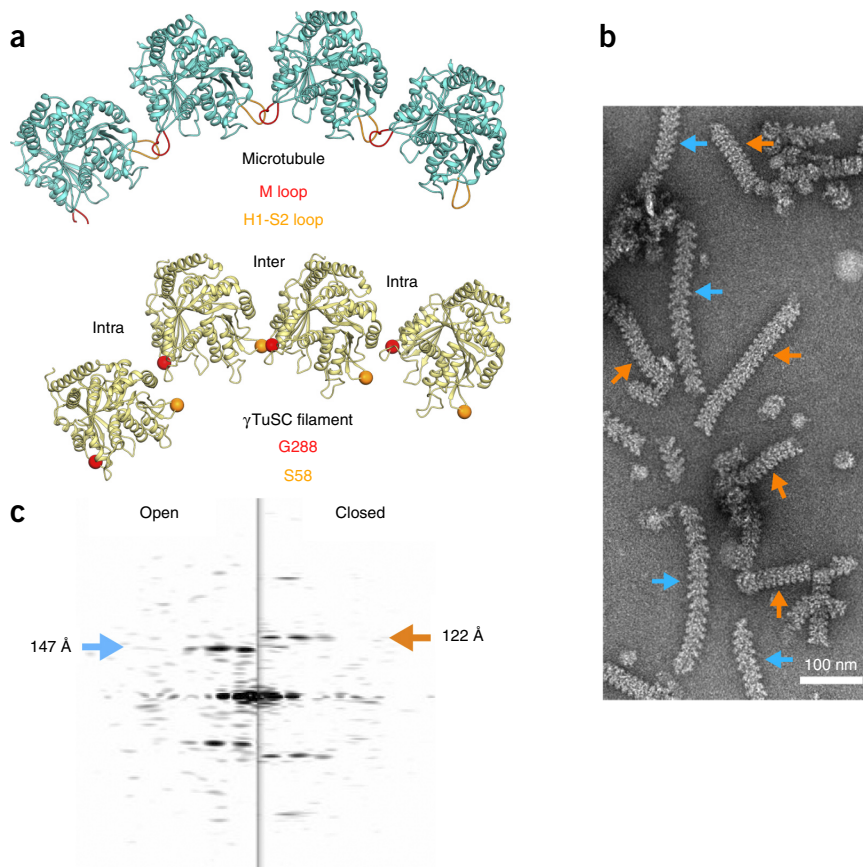


**Figure 1** The yeast  $\gamma$ TuRC is formed from seven  $\gamma$ TuSCs and is limited in size by Spc110. (a) A slice from a tomogram of isolated spindle pole bodies clearly showing the capped minus ends of microtubules (arrows). (b) Subtomogram-averaged structure of microtubule (MT) minus end. Red arrows indicate the position of the half-subunit overlap between the first and seventh  $\gamma$ TuSC (outlined in yellow and orange, respectively). The 120-Å longitudinal rise of the  $\gamma$ TuSC ring is indicated. (c) Micrograph showing assembly of extended filaments by  $\gamma$ TuSC when bound to Spc110<sub>1–220</sub>. Spc110 binds the outer surface of  $\gamma$ TuSC and fits within the groove of the filament (cartoon). (d) Micrograph showing that Spc110<sub>1–401</sub> promotes assembly of  $\gamma$ TuSC rings but prevents extension beyond a single ring.

**Figure 2** Engineered disulfides alter  $\gamma$ TuSC filament morphology. (a) The lateral interface between  $\beta$ -tubulin subunits in the 13-protofilament microtubule and the corresponding lateral interactions between  $\gamma$ -tubulins in the open-state filament. (b) Negative-stain electron micrograph of the double mutant S58C G288C ( $\gamma$ TuSC<sup>CC</sup>) in complex with Spc110<sub>1-220</sub>, showing two distinct filament morphologies (blue and orange arrows). (c) Power spectra showing that individual filaments of different morphologies from **b** have different layer-line spacing indicating different helical pitch.



of one form or the other, thus suggesting a cooperative transition from the open to the closed morphology.

### The structure of closed $\gamma$ TuSC oligomers

We determined the structure of the closed form of  $\gamma$ TuSC<sup>CC</sup>-Spc110<sub>1-220</sub> filaments by cryo-EM and iterative helical real-space reconstruction<sup>19</sup>. To minimize heterogeneity in filament morphology, we extensively dialyzed  $\gamma$ TuSC<sup>CC</sup>-Spc110<sub>1-220</sub> against an oxidizing buffer to promote full disulfide cross-linking (**Supplementary Fig. 3d,e**). We determined an initial structure at 9.4-Å resolution, from about 94,400  $\gamma$ TuSC subunits. To eliminate residual open-closed heterogeneity in the filaments, we sorted the data set by comparing filament segments to the initial  $\gamma$ TuSC<sup>CC</sup> and the open wild-type structures and omitted segments that matched better to the open structure (**Supplementary Fig. 3f**). This yielded a final data set with about 76,000  $\gamma$ TuSC subunits, and a structure at 6.9-Å resolution (**Supplementary Fig. 3g**); the map appears to have anisotropic resolution, with the core density (N-terminal domains of GCP2 and GCP3) more well defined than peripheral densities (C-terminal domains of GCP2 and GCP3, and  $\gamma$ -tubulin).

The refined helical-symmetry parameters for the closed structure ( $-55.4^\circ$  rotation and 18.8-Å rise per subunit, versus  $-54.3^\circ$  rotation and 22.2-Å rise for the open structure) match 13-protofilament-microtubule geometry (**Fig. 3a**) and are a close match to the helical pitch of the subtomogram average of capped minus ends from spindle pole bodies (**Fig. 1b** and **Supplementary Movie 2**). Moreover, in contrast to the staggered pairs of  $\gamma$ -tubulins in the open state, the intra- and inter- $\gamma$ TuSC lateral contacts are very similar to each other and closely resemble the microtubule lattice (**Fig. 3b**). Thus, in a single turn of the closed state, the ring of  $\gamma$ -tubulins is positioned to act as a nearly perfect microtubule template.

### The closed conformation enhances nucleation activity

The similarity to the microtubule lattice suggested that the nucleating activity of  $\gamma$ TuSC would be enhanced in the closed state. We tested the difference in activity between the open and closed states with solution nucleation assays. We previously tested the nucleation activity of  $\gamma$ TuSC in the context of filaments formed in the presence of Spc110<sub>1-220</sub> (ref. 10). This probably underestimated the full activity because only  $\gamma$ TuSCs at the end of a filament would have been accessible for interaction with  $\alpha\beta$ -tubulin. Here, we used individual  $\gamma$ TuSCs in which all of the  $\gamma$ -tubulin is available for interaction

with  $\alpha\beta$ -tubulin, formed with the longer Spc110<sub>1-401</sub> construct that promotes assembly but blocks filament extension (**Fig. 1d**).

We compared nucleating activity of reduced and oxidized single rings of  $\gamma$ TuSC-Spc110<sub>1-401</sub> and  $\gamma$ TuSC<sup>CC</sup>-Spc110<sub>1-401</sub>. Assays performed with mammalian brain tubulin showed only a two- to three-fold increase in activity over buffer controls when we used assembled yeast  $\gamma$ TuSCs<sup>10</sup>. Given the quality of the symmetry match, we became concerned that there could be some problem in using mammalian tubulin with yeast  $\gamma$ TuSCs. So, despite general assumptions of strong conservation of tubulins across species, we repeated these assays with wild-type  $\gamma$ TuSC and purified recombinant *S. cerevisiae*  $\alpha\beta$ -tubulin<sup>20</sup>. With yeast tubulin we observed an approximately 300-fold increase in the number of microtubules (**Fig. 3c,d**), results indicating a remarkably strong species-specificity in the  $\gamma$ TuSC- $\alpha\beta$ -tubulin interaction (**Supplementary Fig. 4a**).

We tested the activities of  $\gamma$ TuSC and  $\gamma$ TuSC<sup>CC</sup> under reducing (open) and oxidizing (closed) conditions. Wild-type  $\gamma$ TuSC had similar nucleation rates under both conditions, whereas  $\gamma$ TuSC<sup>CC</sup> nucleation was similar to that of wild-type under reducing conditions, but it doubled under oxidizing conditions (**Fig. 3c,d**). Thus, artificially forcing the geometry of the  $\gamma$ TuSC ring to better match that of the microtubule results in enhanced nucleating activity. Although the improvement demonstrates the importance of geometric fidelity, the modest increase suggests that other conformational changes, such as a curved-to-straight transition within the  $\gamma$ -tubulin<sup>19</sup>, may be required to fully activate the complex.

### Pseudoatomic model of $\gamma$ TuSC

We generated a pseudoatomic model of  $\gamma$ TuSC by fitting and refining homology models of  $\gamma$ -tubulin, GCP2 and GCP3 into the cryo-EM density of a single closed-state  $\gamma$ TuSC subunit (**Fig. 4a,b**) and the

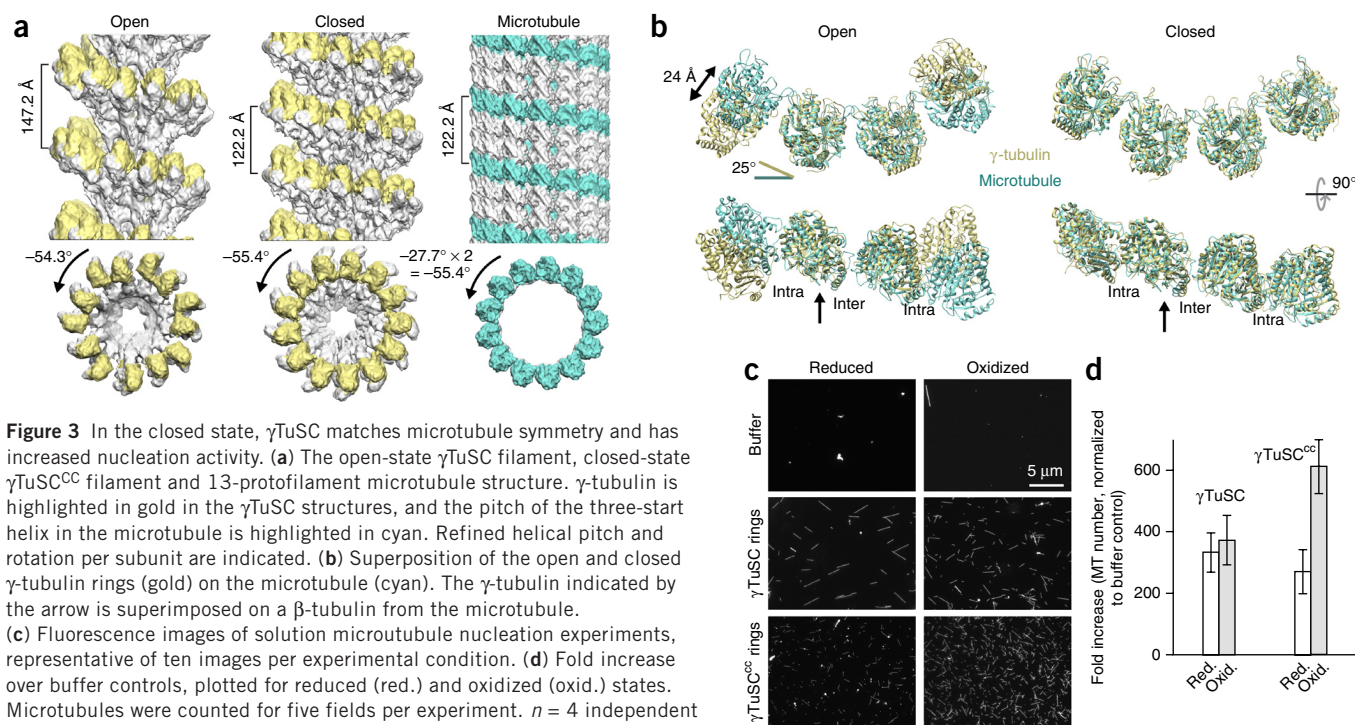


**Figure 3** In the closed state,  $\gamma$ TuSC matches microtubule symmetry and has increased nucleation activity. (a) The open-state  $\gamma$ TuSC filament, closed-state  $\gamma$ TuSC<sup>cc</sup> filament and 13-protofilament microtubule structure.  $\gamma$ -tubulin is highlighted in gold in the  $\gamma$ TuSC structures, and the pitch of the three-start helix in the microtubule is highlighted in cyan. Refined helical pitch and rotation per subunit are indicated. (b) Superposition of the open and closed  $\gamma$ -tubulin rings (gold) on the microtubule (cyan). The  $\gamma$ -tubulin indicated by the arrow is superimposed on a  $\beta$ -tubulin from the microtubule. (c) Fluorescence images of solution microtubule nucleation experiments, representative of ten images per experimental condition. (d) Fold increase over buffer controls, plotted for reduced (red.) and oxidized (oxid.) states. Microtubules were counted for five fields per experiment.  $n = 4$  independent experiments; error bars, s.e.m. Significant differences between activity of  $\gamma$ TuSC110<sup>cc</sup> complexes under oxidizing and reducing conditions ( $P \leq 0.013$ ) or between mutant and wild-type ( $P \leq 0.055$ ) were confirmed by two-tailed  $t$  test. The activity of  $\gamma$ TuSCs alone was similar to buffer controls, with only a few microtubules on the entire coverslip (data not shown).

lower-resolution open state that we determined previously<sup>10</sup>. We faced several challenges in generating the model: the very low sequence identity between GCP2 and GCP3 with GCP4 (the only homolog with a crystal structure determined) made generating reliable homology models difficult; GCP2 and GCP3 are in different conformations than GCP4; and the anisotropic resolution of the EM structure led to less reliable fitting of the C-terminal domains of GCP2 and GCP3 and  $\gamma$ -tubulin. We developed several new tools to perform the modeling and to validate the model; the approach is outlined below in Online Methods, and a full description of the modeling procedure will be described elsewhere.

GCP2 and GCP3, which have similar overall shapes, have been distinguished by previous labeling experiments<sup>1</sup>. The primary difference between the open and closed states is the degree of flexing in GCP2 and GCP3. Both change conformation, with GCP3 straightening by about  $9^\circ$  and GCP2 bending by about  $8^\circ$  in the closed state (Supplementary Fig. 5a). In the closed state, GCP2 and GCP3 are similar to each other and to the human GCP4 crystal structure,

whereas GCP2 and GCP3 are in different flexed conformations in the open state (Supplementary Fig. 5b–e).

Density in the EM map that we previously suggested corresponds to part of Spc110 (ref. 10) is more easily resolved in the new higher-resolution map, and it clearly resembles a two-stranded coiled coil. The model includes 44 residues of Spc110 as a generic two-stranded coiled coil (Fig. 4a). This density makes contacts with N-terminal regions of GCP2 and GCP3, with the closest contacts near the base of GCP2 and the side of the coiled coil. Near the top (as depicted in Supplementary Fig. 5f), the Spc110 density splays apart, with one strand bending back toward GCP3 and the other extending away from GCP2 toward a  $\gamma$ -tubulin in the next layer of the helix. This model accounts for about 20% of the mass of the Spc110<sub>1–220</sub> construct. Much of the remainder of the molecule is probably near the center of the filament, where the ordered density on the outer surface connects to disordered density that runs through the core of the structure (Supplementary Fig. 5g). This positioning of Spc110 is consistent with the fact that longer lengths of coiled coil inhibit

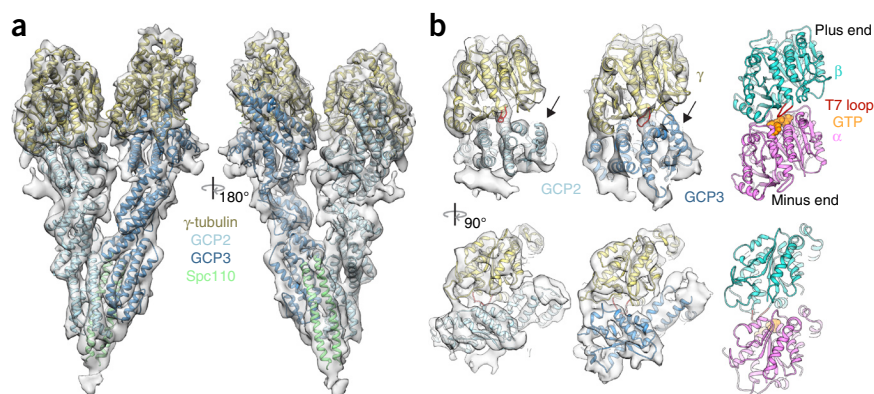
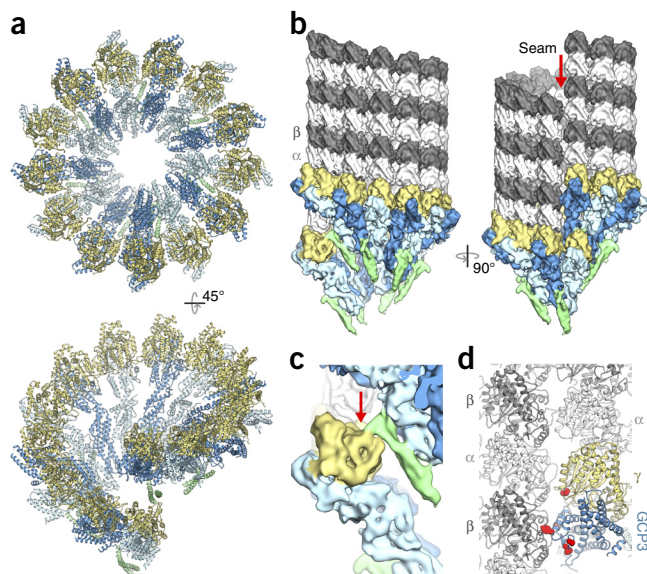


**Figure 4** Pseudoatomic model of  $\gamma$ TuSC in the closed conformation. (a) Pseudoatomic model of  $\gamma$ TuSC (ribbon diagram) fit into the cryo-EM structure (semitransparent surface). (b) Close up views of the interactions of  $\gamma$ -tubulin with the C-terminal domains of GCP2 and GCP3, compared to longitudinal interactions within the  $\alpha\beta$ -tubulin heterodimer, with the T7 loop highlighted in red. The top view is the view from inside the microtubule, and the bottom view is of the lateral interaction surfaces. Contacts are made between the H1-S2 loop of  $\gamma$ -tubulin and residues 524–536 of GCP3; the corresponding region of GCP2 is shifted away from  $\gamma$ -tubulin in the GCP2 structure (arrows).

**Figure 5** Pseudoatomic model of  $\gamma$ TuRC and its interactions with microtubules. (a) Pseudoatomic model of a complete yeast  $\gamma$ TuRC with seven  $\gamma$ TuSCs. (b) A model of yeast  $\gamma$ TuRC interacting with the minus end of a microtubule. (c) A potential contact between the last  $\gamma$ -tubulin in the ring, which is not directly interacting with the microtubule, and Spc110 bound to the first  $\gamma$ TuSC (arrow) in the  $\gamma$ TuSC<sup>CC</sup> structure. (d) Magnified view of interactions between the first  $\gamma$ TuSC and the microtubule. Known phosphorylation sites on  $\gamma$ TuSC that could potentially modulate lateral interactions with  $\alpha\beta$ -tubulin are indicated with red spheres.



filament elongation (Fig. 1d), because adding additional mass to the center of the filament would probably disrupt the helical packing.

The model also provides new insights into the contacts between  $\gamma$ -tubulin and GCP2 and GCP3 (Fig. 4b). Both GCP2 and GCP3 C-terminal domains make contacts with the minus-end longitudinal surface of  $\gamma$ -tubulin, with the strongest contacts made with the T7 loop of  $\gamma$ -tubulin. The major difference between GCP2 and GCP3 in their interactions with  $\gamma$ -tubulin is an interaction between the H1-S2 loop of  $\gamma$ -tubulin with a loop in GCP3; the corresponding region of GCP2 is shifted away from  $\gamma$ -tubulin (Fig. 4b). The H1-S2 loop is at the lateral  $\gamma$ -tubulin interaction surface, and the interactions with GCP3 may serve to modulate lateral interactions.

## DISCUSSION

The conformational change from the open to the closed form of  $\gamma$ TuSC is driven by flexing of GCP2 and GCP3, distant homologs of GCP4. In the open state, the conformations of both GCP2 and GCP3 differ from that of GCP4, whereas in the closed state all three are in similar conformations (Supplementary Fig. 5a–e). This suggests that specific evolutionary changes in GCP2 and GCP3 have stabilized their open, less active, conformations. The advantage of stabilizing the lower-activity state would be the ability to rapidly and specifically upregulate  $\gamma$ TuRC activity through allosteric activation.

The closed state is about twice as active as the open state, thus indicating that nucleating activity can be modulated by  $\gamma$ TuSC conformation (Fig. 3). Importantly, yeast  $\gamma$ TuRC demonstrated strong species specificity, being about 100-fold more active with yeast tubulin than with vertebrate tubulin. Previous nucleation assays, all performed with mammalian brain tubulin, found animal  $\gamma$ TuRC to be much more active than the yeast counterpart<sup>3,10,21,22</sup>. However, we observed similar activity levels when the tubulin and  $\gamma$ TuRC species were matched, results emphasizing the importance of pairing tubulin and  $\gamma$ TuRC from the same species in microtubule nucleation assays (Supplementary Fig. 4a). A number of amino acid substitutions between vertebrate and yeast sequences at the  $\alpha$ -tubulin– $\gamma$ -tubulin contact surfaces may account for the species specificity (Supplementary Fig. 4b–d).

The modest two-fold increase in activity that we see on transition to the closed state is in line with enhancement levels previously observed with  $\gamma$ TuRC-activating proteins in metazoans. The addition of CDK5RAP2 activating protein to isolated human  $\gamma$ TuRCs resulted in five-fold enhancement of activity. Overexpression or depletion of CDK5RAP2 resulted in large-scale changes to the microtubule cytoskeleton in cells, thus suggesting that small shifts in the activity of the nucleating complex can have a large impact on cytoskeletal organization<sup>22</sup>. It is also possible that, in our artificial cross-linked system, other potentially important allosteric activations are not being recapitulated. For example,  $\alpha\beta$ -tubulin undergoes a dramatic curved-to-straight conformational change upon polymerization<sup>23,24</sup>, and a similar transition may accompany normal closure of  $\gamma$ TuSC but may not be induced in our cross-linked system; this would result in underestimation of the enhancement of nucleation in a natively closed structure.

A single turn of the  $\gamma$ TuSC<sup>CC</sup> closed state provides a model for the full  $\gamma$ TuRC (Fig. 5a). From this, we extrapolated a structural model of  $\gamma$ TuRC bound to a microtubule, assuming that longitudinal contacts between  $\gamma$ -tubulin and  $\alpha$ -tubulin are similar to the  $\alpha$ -tubulin– $\beta$ -tubulin contacts (Fig. 5b and Supplementary Movie 3). This model, in both overall morphology and helical symmetry, is remarkably similar to the microtubule minus end that we observed in SPBs. In the model, 13  $\gamma$ -tubulins make contact with the microtubule; a 14th  $\gamma$ -tubulin, bound to GCP2 in the terminal  $\gamma$ TuSC, lies directly below the first  $\gamma$ -tubulin but does not make contact with the microtubule. Intriguingly, a new interaction appeared between one end of the ordered Spc110 density and the H6-H7 loop of the 14th  $\gamma$ -tubulin, suggesting a possible role for Spc110 in stabilizing the  $\gamma$ TuRC ring at this overlapping position (Fig. 5c). In addition to the 13 longitudinal contacts between  $\gamma$ -tubulin and  $\alpha$ -tubulin around the ring, the model predicts a single lateral contact between  $\alpha$ -tubulin and  $\gamma$ -tubulin at the first position in the ring; a lateral interaction between the GCP3 C-terminal domain and an adjacent  $\beta$ -tubulin may also occur here (Fig. 5d).

A large number of phosphorylation sites have been identified on  $\gamma$ -tubulin, GCP2 and GCP3 in *S. cerevisiae*<sup>25–30</sup>. Phosphorylation at a few sites has been shown to affect organization of the mitotic spindle<sup>28,30,31</sup>, but the functional roles of most sites remain unknown. Mapping of the sites on the  $\gamma$ TuRC model shows that they fall broadly into three categories: on the exterior of the  $\gamma$ TuRC, at the exposed plus end of  $\gamma$ -tubulin and on the interior of the  $\gamma$ TuRC (Supplementary Fig. 6). Exterior sites may be involved in modulating  $\gamma$ TuRC interaction with binding partners, potentially affecting localization or activation. Sites at the plus end of  $\gamma$ -tubulin would be expected to directly modulate interactions with  $\alpha\beta$ -tubulin; similarly, sites at the lateral contact surfaces between GCP3 or  $\gamma$ -tubulin and  $\alpha\beta$ -tubulin may directly influence microtubule interactions (Fig. 5d). The phosphorylation sites on the ring interior, lying mostly near the minus end of  $\gamma$ -tubulin, would probably be inaccessible to kinases when  $\gamma$ TuRC is bound to a microtubule, thus suggesting that phosphorylation at these sites occurs when  $\gamma$ TuRCs are unoccupied or possibly before assembly of  $\gamma$ TuSCs into  $\gamma$ TuRC, and it may serve to downregulate nucleation activity.

The transition from an open to a closed state is likely to provide an allosteric mechanism for modulating  $\gamma$ TuSC activity. It remains to be seen what factor or factors are involved in promoting this transition

*in vivo*, and post-translational modification of  $\gamma$ TuSC components<sup>28,31</sup> or direct binding by regulatory proteins may be required<sup>22,32,33</sup>. Regulation of  $\gamma$ TuRC at the levels of  $\gamma$ TuSC assembly, post-translational modification and open-to-closed conformation are all likely to be involved in providing precise control of nucleating activity.

## METHODS

Methods and any associated references are available in the [online version of the paper](#).

**Accession codes.** The structures of the capped microtubule end and  $\gamma$ TuSC<sup>CC</sup>-Spc110<sub>1–220</sub> filament have been deposited in the Electron Microscopy Data Bank under accession numbers [EMD-5989](#) and [EMD-2799](#), respectively.

*Note: Any Supplementary Information and Source Data files are available in the [online version of the paper](#).*

## ACKNOWLEDGMENTS

The authors are grateful to M. Braunfeld and X. Li for assistance with cryo-EM data collection and L. Rice for help with overexpression and purification of yeast tubulin. This work was funded by the Howard Hughes Medical Institute and by US National Institutes of Health grants R01 GM031627 to D.A.A., R01 GM040506 to T.N.D. and T32 GM007270 to K.K.F.

## AUTHOR CONTRIBUTIONS

J.M.K. prepared samples, collected cryo-EM data, performed three-dimensional reconstructions, analyzed data and wrote the paper. C.H.G. performed molecular modeling, analyzed results and contributed to writing the paper. S.L. prepared samples, collected tomographic data, performed tomographic reconstructions and analyzed data. M.M. performed microtubule nucleation assays and analyzed data. A.Z. generated expression constructs and optimized protein expression. K.K.F. performed yeast viability assays and spindle morphology experiments and analyzed data. J.-J.F. assisted with subvolume averaging. A.S. analyzed data and contributed to writing the paper. J.K. provided samples and analyzed data. T.N.D. analyzed data and contributed to writing the paper. D.A.A. analyzed data and contributed to writing the paper.

## COMPETING FINANCIAL INTERESTS

The authors declare no competing financial interests.

Reprints and permissions information is available online at <http://www.nature.com/reprints/index.html>.

- Choy, R.M., Kollman, J.M., Zelter, A., Davis, T.N. & Agard, D.A. Localization and orientation of the  $\gamma$ -tubulin small complex components using protein tags as labels for single particle EM. *J. Struct. Biol.* **168**, 571–574 (2009).
- Kollman, J.M. *et al.* The structure of the  $\gamma$ -tubulin small complex: implications of its architecture and flexibility for microtubule nucleation. *Mol. Biol. Cell* **19**, 207–215 (2008).
- Oegema, K. *et al.* Characterization of two related *Drosophila*  $\gamma$ -tubulin complexes that differ in their ability to nucleate microtubules. *J. Cell Biol.* **144**, 721–733 (1999).
- Zheng, Y., Wong, M.L., Alberts, B. & Mitchison, T. Nucleation of microtubule assembly by a  $\gamma$ -tubulin-containing ring complex. *Nature* **378**, 578–583 (1995).
- Kollman, J.M., Merdes, A., Mourey, L. & Agard, D.A. Microtubule nucleation by  $\gamma$ -tubulin complexes. *Nat. Rev. Mol. Cell Biol.* **12**, 709–721 (2011).
- Moritz, M., Braunfeld, M.B., Guenebaut, V., Heuser, J. & Agard, D.A. Structure of the  $\gamma$ -tubulin ring complex: a template for microtubule nucleation. *Nat. Cell Biol.* **2**, 365–370 (2000).
- Oakley, B.R., Oakley, C.E., Yoon, Y. & Jung, M.K.  $\gamma$ -tubulin is a component of the spindle pole body that is essential for microtubule function in *Aspergillus nidulans*. *Cell* **61**, 1289–1301 (1990).
- Kilmartin, J.V. & Goh, P.Y. Spc110p: assembly properties and role in the connection of nuclear microtubules to the yeast spindle pole body. *EMBO J.* **15**, 4592–4602 (1996).
- Sundberg, H.A. & Davis, T.N. A mutational analysis identifies three functional regions of the spindle pole component Spc110p in *Saccharomyces cerevisiae*. *Mol. Biol. Cell* **8**, 2575–2590 (1997).
- Kollman, J.M., Polka, J.K., Zelter, A., Davis, T.N. & Agard, D.A. Microtubule nucleating  $\gamma$ -TuSC assembles structures with 13-fold microtubule-like symmetry. *Nature* **466**, 879–882 (2010).
- Tilney, L.G. *et al.* Microtubules: evidence for 13 protofilaments. *J. Cell Biol.* **59**, 267–275 (1973).
- O'Toole, E.T., Winey, M. & McIntosh, J.R. High-voltage electron tomography of spindle pole bodies and early mitotic spindles in the yeast *Saccharomyces cerevisiae*. *Mol. Biol. Cell* **10**, 2017–2031 (1999).
- Erlmann, S. *et al.* An extended  $\gamma$ -tubulin ring functions as a stable platform in microtubule nucleation. *J. Cell Biol.* **197**, 59–74 (2012).
- Sui, H. & Downing, K.H. Structural basis of interprotofilament interaction and lateral deformation of microtubules. *Structure* **18**, 1022–1031 (2010).
- Keating, T.J. & Borisy, G.G. Immunostuctural evidence for the template mechanism of microtubule nucleation. *Nat. Cell Biol.* **2**, 352–357 (2000).
- Wiese, C. & Zheng, Y. A new function for the  $\gamma$ -tubulin ring complex as a microtubule minus-end cap. *Nat. Cell Biol.* **2**, 358–364 (2000).
- Aldaz, H., Rice, L.M., Stearns, T. & Agard, D.A. Insights into microtubule nucleation from the crystal structure of human  $\gamma$ -tubulin. *Nature* **435**, 523–527 (2005).
- Rice, L.M., Montabana, E.A. & Agard, D.A. The lattice as allosteric effector: structural studies of  $\alpha$ - and  $\gamma$ -tubulin clarify the role of GTP in microtubule assembly. *Proc. Natl. Acad. Sci. USA* **105**, 5378–5383 (2008).
- Egelman, E.H. The iterative helical real space reconstruction method: surmounting the problems posed by real polymers. *J. Struct. Biol.* **157**, 83–94 (2007).
- Johnson, V., Ayaz, P., Huddleston, P. & Rice, L.M. Design, overexpression, and purification of polymerization-blocked yeast  $\alpha$ -tubulin mutants. *Biochemistry* **50**, 8636–8644 (2011).
- Vinh, D.B., Kern, J.W., Hancock, W.O., Howard, J. & Davis, T.N. Reconstitution and characterization of budding yeast  $\gamma$ -tubulin complex. *Mol. Biol. Cell* **13**, 1144–1157 (2002).
- Choi, Y.K., Liu, P., Sze, S.K., Dai, C. & Qi, R.Z. CDK5RAP2 stimulates microtubule nucleation by the  $\gamma$ -tubulin ring complex. *J. Cell Biol.* **191**, 1089–1095 (2010).
- Löwe, J., Li, H., Downing, K.H. & Nogales, E. Refined structure of  $\alpha$ -tubulin at 3.5 Å resolution. *J. Mol. Biol.* **313**, 1045–1057 (2001).
- Ravelli, R.B. *et al.* Insight into tubulin regulation from a complex with colchicine and a stathmin-like domain. *Nature* **428**, 198–202 (2004).
- Holt, L.J. *et al.* Global analysis of Cdk1 substrate phosphorylation sites provides insights into evolution. *Science* **325**, 1682–1686 (2009).
- Albuquerque, C.P. *et al.* A multidimensional chromatography technology for in-depth phosphoproteome analysis. *Mol. Cell. Proteomics* **7**, 1389–1396 (2008).
- Holinger, E.P. *et al.* Budding yeast centrosome duplication requires stabilization of Spc29 via Mps1-mediated phosphorylation. *J. Biol. Chem.* **284**, 12949–12955 (2009).
- Keck, J.M. *et al.* A cell cycle phosphoproteome of the yeast centrosome. *Science* **332**, 1557–1561 (2011).
- Lin, T.C. *et al.* Phosphorylation of the yeast  $\gamma$ -tubulin Tub4 regulates microtubule function. *PLoS ONE* **6**, e19700 (2011).
- Vogel, J. *et al.* Phosphorylation of  $\gamma$ -tubulin regulates microtubule organization in budding yeast. *Dev. Cell* **1**, 621–631 (2001).
- Nazarova, E. *et al.* Distinct roles for antiparallel microtubule pairing and overlap during early spindle assembly. *Mol. Biol. Cell* **24**, 3238–3250 (2013).
- Samejima, I., Miller, V.J., Grocock, L.M. & Sawin, K.E. Two distinct regions of Mto1 are required for normal microtubule nucleation and efficient association with the  $\gamma$ -tubulin complex *in vivo*. *J. Cell Sci.* **121**, 3971–3980 (2008).
- Goshima, G., Mayer, M., Zhang, N., Stuurman, N. & Vale, R.D. Augmin: a protein complex required for centrosome-independent microtubule generation within the spindle. *J. Cell Biol.* **181**, 421–429 (2008).

## ONLINE METHODS

**Spindle pole body purification and imaging.** Spindle pole bodies from *Saccharomyces cerevisiae* were purified according to previously published procedures<sup>34,35</sup>. The purified SPB sample, initially in a high concentration of sucrose, was first dialyzed at 4 °C overnight in a buffer containing 10 mM bis-Tris-Cl, pH 6.5, 0.1 mM MgCl<sub>2</sub>, and 20% (v/v) DMSO. The next day, after being mixed with 10 nm colloidal gold, the sample was applied onto either a homemade holey carbon grid or a Quantifoil grid (PSI) in a humidity chamber, then blotted and plunged into liquid ethane with either a homemade plunger or a Vitrobot (FEI). Frozen grids were stored in liquid nitrogen before use. Tomography data were collected on a Polara electron microscope (FEI) running at 300 kV. A postcolumn energy filter (GIF, Gatan) was used, and the slit width was set at 25 eV. Automatic data collection was carried out with UCSF Tomography software<sup>36</sup>. Single-axis tilt series were collected at a nominal magnification of 41,000. Images of dimension 2,032 × 2,032 were recorded on a CCD camera (UltraCam, Gatan). The final pixel size on the images was 5.32 Å. The specimen was tilted from -60° to +60° in 1.5° steps. The microscope defocus values were set in the range of 10 to 15 μm. The accumulated dose for each tilt series was ~60 e<sup>-</sup>/Å<sup>2</sup>.

**Subvolume averaging of capped minus ends.** For averaging γ-TuRC, the minus-end caps of microtubules attached to the nuclear face of the spindle pole body were identified manually. A total of 1,156 subtomograms containing the MT minus end were selected from 61 tomograms. They were boxed out and subjected to reference-free alignment by either a maximum-likelihood algorithm in the Xmipp package<sup>37</sup> or a constrained cross-correlation algorithm<sup>38</sup>. The alignment was carried out progressively with improvement in resolution. The structure converged after about five rounds of iterations.

**Generation of γTuSC<sup>CC</sup> and Spc110<sub>1-401</sub> expression vectors.** Spc110<sub>1-401</sub> was generated from Spc110 and GST DNA from the Spc110-GST pFastBac vector<sup>21</sup>. Primers were designed to amplify the Spc110<sub>1-401</sub> coding sequence while adding a BamHI site immediately upstream of the open reading frame and a PstI site immediately downstream of the 401st Spc110 codon. Primers were designed to amplify the GST coding sequence while adding a PstI site followed by a TEV-cleavage site immediately upstream of the GST open reading frame as well as a HindIII site immediately downstream of the GST stop codon. The resulting PCR products were cloned into the Invitrogen Zero Blunt TOPO vector according to the manufacturer's instructions. BamHI and PstI were used to excise Spc110<sub>1-401</sub>, and HindIII and PstI were used to excise TEV-GST from their respective TOPO vectors. The resulting fragments were ligated into pFastBac (Invitrogen) linearized with HindIII and BamHI. The Bac-to-Bac baculovirus expression system (Invitrogen) was used to produce protein from Sf9 cells according to the manufacturer's instructions with Sf-900 II SFM liquid medium (Invitrogen) supplemented with 2.5% FBS.

To generate γTuSC<sup>CC</sup>, S58 and G288 of γ-tubulin were mutated to cysteines with the QuikChange Multi Site-Directed Mutagenesis Kit (Agilent Technologies) according to the manufacturer's instructions. The resulting mutant sequence was PCR amplified and cloned into the Invitrogen Zero Blunt TOPO vector according to the manufacturer's instructions. XhoI and HindIII were used to excise the mutant Tub4 sequence. The resulting fragment was ligated into pFastBac (Invitrogen) linearized with the same enzymes.

For viability testing, integrating vectors based on the pRS306 (ref. 39) backbone were constructed. These contained either wild-type or mutant (S58C G288C) Tub4. 432 bp of upstream and 334 bp of downstream flanking genomic DNA sequence were included in the vector surrounding the Tub4 coding sequence.

**Preparation of recombinant γTuSC and γTuSC complexes.** γTuSC or γTuSC<sup>CC</sup> was coexpressed with GST-tagged Spc110 constructs in Sf9 cells and purified as previously described<sup>10</sup>. Briefly, cell lysate was incubated with glutathione resin, washed in H100 (40 mM HEPES, pH 7.6, 100 mM KCl, 1 mM EGTA, and 1 mM MgCl<sub>2</sub>) and eluted from the resin by cleavage of the GST tag with TEV protease as the final purification step. For cryo-EM, γTuSC<sup>CC</sup>-Spc110<sub>1-220</sub> filaments were at 2 mg/ml total protein in H100 and 1 mM oxidized glutathione. Negative-stain samples were prepared as previously described<sup>40</sup> in 0.75% uranyl formate, and cryo-EM samples were prepared on C-FLAT holey carbon grids<sup>41</sup> with a Vitrobot (FEI).

**Imaging and three-dimensional reconstruction of γTuSC and γTuSC complexes.** Negative-stain samples were imaged on a Tecnai Spirit G<sup>2</sup> Biotwin electron microscope (FEI) operating at 120 kV, and images were recorded on an UltraScan 4000 CCD detector (Gatan). Cryo-EM images were recorded on a Tecnai TF20 electron microscope operating at 200 kV, and images were recorded on an 8,000 × 8,000 TemCam-F816 camera (TVIPS, GmbH) with a pixel size of 0.94 Å/pixel. Images were acquired in a defocus range of 0.8–2 μm. Defocus was determined with CTFIND<sup>42</sup>, and each micrograph was corrected by application of a Wiener filter. Particles were boxed out in 485-Å segments, overlapping by 448 Å. After several initial rounds of unrestrained alignment search, the particles were centered with respect to the helix axis by integer pixel shifts.

Iterative helical real-space reconstruction was performed essentially as previously described by Egelman<sup>43</sup> and Sasche *et al.*<sup>44</sup>, with SPIDER<sup>45</sup>, with a low-pass-filtered cylinder used as the initial reference volume. Initial helical symmetry parameters were taken from the open-state γTuSC filament (-54.3° rotation, 22.2-Å rise per subunit) and refined at each iteration with hsearch\_lorenz<sup>43</sup>. Initial centering of the particles was carried out on 4×-binned images, with subsequent refinement on 2×-binned images. An initial structure was determined at ~9.6-Å resolution. To reduce open-to-closed heterogeneity in the data set, cross correlations were calculated for each helical segment to the initial reconstruction and the original open-state structure<sup>10</sup>, and particles matching better to the open state were omitted from further rounds of refinement. After sorting, five rounds of unrestrained alignment search were carried out with the 2×-binned images. To minimize effects of bending in the helix, each segment was masked to 200 Å along the helical axis and 340 Å perpendicular to the axis with a cosine-edged mask. These masked particles were then subjected to five rounds of local refinement of the unbinned images. Resolution was assessed by the FSC<sub>0.5</sub> criterion. Volumes were viewed and segmented with Chimera<sup>46</sup>.

**Fluorescence imaging of yeast cells carrying the γTuSC<sup>CC</sup> mutation.** All yeast strains were derived from W303. Fluorescent tags were introduced by PCR as described ([http://depts.washington.edu/yeastrc/pages/plasmids\\_protocols.html](http://depts.washington.edu/yeastrc/pages/plasmids_protocols.html)), and *TUB4*(S58C G288C) was integrated at the *TUB4* locus into *glr1Δ* cells, which carry a deletion for the gene encoding glutathione reductase and have high levels of oxidized glutathione<sup>47</sup>. The *glr1Δ* strain was used to increase the favorability of forming disulfides in the *TUB4* mutant. Live cells were mounted for microscopy on a 1% agarose pad<sup>48</sup>. Images were acquired at a single focal plane, with 1×1 binning, with a U Plan Apo 100× objective lens (1.35 NA), an Olympus IX70 inverted microscope, and a CoolSnap HQ digital camera (Photometrics) managed by softWorX software (Applied Precision). Exposures were 0.4 s for both mCherry and GFP. The images were processed as previously described<sup>49</sup> with custom Matlab programs (available upon request) to identify and quantify mCherry and GFP fluorescence intensities.

**Yeast strains used.** All yeast strains also have *ade2-1oc ade3Δ-100 can1-100 his3-11,15 leu2-3,112 trp1-1 ura3-1* except as shown. Yeast strains used were KFY36-13C, *MATα LEU2::GFP-TUB1 lys2Δ::HIS3 SPC42-mCherry::hphMX*; KFY42-1C, *MATα, LEU2::GFP-TUB1 lys2Δ::HIS3 glr1Δ::TRP1 SPC42-mCherry::hphMX*; KFY91, *MATα, LEU2::GFP-TUB1 lys2Δ::HIS3 glr1Δ::TRP1 SPC42-mCherry::hphMX TUB4(S58C G288C)*; KFY135-8B, *MATα lys2Δ::HIS3 TUB4(S58C G288C)::URA3::tub4Δ::kanMX glr1Δ::TRP1 SPC42-mCherry::hphMX NUF2-GFP::kanMX*; KFY135-47A, *MATα glr1Δ::TRP1 SPC42-mCherry::hphMX NUF2-GFP::kanMX*; and KFY138-5A, *MATα NUF2-GFP::kanMX SPC42-mCherry::hphMX*.

**Microtubule nucleation assays.** Yeast tubulin was overexpressed and purified as previously described<sup>20</sup>. Pure γTuSC-Spc110, γTuSC alone, or buffer control (40 mM K-HEPES, pH 6.9, 100 mM KCl, 1 mM EGTA, 1 mM MgCl<sub>2</sub>, 20% glycerol, 100 μM GTP, and 100 μM oxidized or reduced glutathione) and *S. cerevisiae* tubulin were diluted at the appropriate concentrations into microtubule assembly buffer (80 mM K-PIPES, pH 6.9, 125 mM KCl, 20% glycerol, 1 mM EGTA, 1 mM MgCl<sub>2</sub>, 1 mM GTP, and 100 μM oxidized or reduced glutathione) on ice. Reactions were incubated at 30 °C for 20 min, fixed 3 min in ten volumes of 1% glutaraldehyde in BRB80 (80 mM K-PIPES, pH 6.9, 1 mM EGTA, and 1 mM MgCl<sub>2</sub>) and then diluted ten times into BRB80 (final volume 1.5 ml). 1 ml of the resulting fixed reactions was layered onto 20% glycerol/BRB80 cushions and centrifuged for 45 min, at 24,000g, onto 18-mm round coverslips.

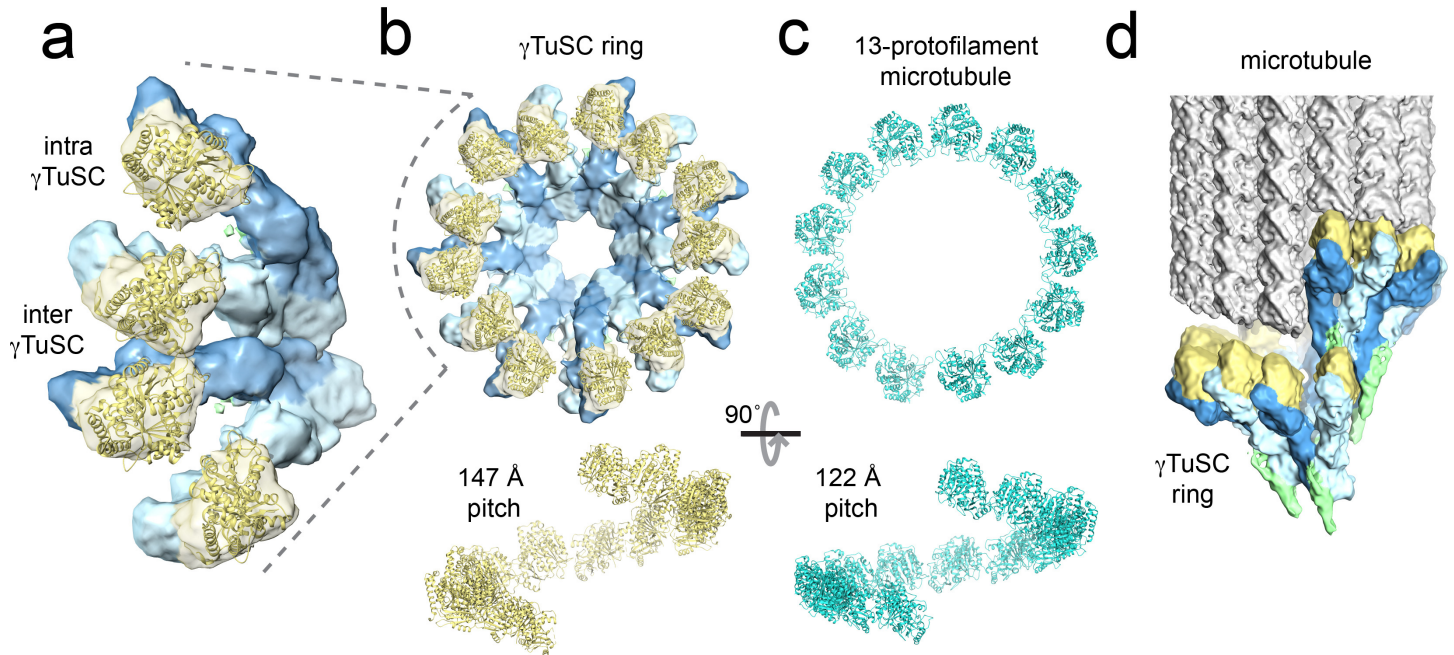
Microtubules were visualized on the coverslips by immunofluorescence with FITC-labeled mouse anti- $\alpha$ -tubulin (Sigma F2168, validation provided on manufacturer's website) at 1:500 dilution, and 5–10 fields of microtubules were counted for each experiment.

**Homology modeling and flexible fitting.** Models of  $\gamma$ TuSC were computed with a combination of comparative protein structure modeling and flexible fitting into the EM density map of the closed state. To create a template structure for  $\gamma$ TuSC, we rigidly docked two copies of the crystal structure of human GCP4 into the density map with UCSF Chimera<sup>46</sup>. Independently, initial alignment of the sequences in the TUBGCP family was performed with Promals3D<sup>50</sup>. Next, we produced an initial homology model of the GCP2–GCP3 dimer based on the initial alignment and the GCP4 template, with MODELLER 9.13 (ref. 51). The alignment was then iteratively refined by hand to improve the fit of the model into the density map. With the final alignment, 200 homology models of the dimer were produced. We completed each dimer into a model of  $\gamma$ TuSC by rigidly docking two copies of  $\gamma$ -tubulin and a coiled-coil fragment of Spc110. An additional neighboring copy of the complete  $\gamma$ TuSC structure was added to model the inter- $\gamma$ TuSC interface. Subsequently, each  $\gamma$ TuSC dimer was flexibly fitted into the density map with MDFF<sup>52</sup>, with additional restraints to preserve helical symmetry, secondary structure, and conformation of the  $\gamma$ -tubulin domains. The best-scoring model, as defined by the highest cross-correlation coefficient between the model and the map, was subjected to additional local sampling to estimate model precision, with MODELLER to randomize loops and MDFF to reoptimize the structures. The above process was repeated for the open state, with the open-state EM density map and the final alignment from the modeling of the closed state.

34. Rout, M.P. & Kilmartin, J.V. Yeast spindle pole body components. *Cold Spring Harb. Symp. Quant. Biol.* **56**, 687–692 (1991).
35. Donaldson, A.D. & Kilmartin, J.V. Spc42p: a phosphorylated component of the *S. cerevisiae* spindle pole body (SPB) with an essential function during SPB duplication. *J. Cell Biol.* **132**, 887–901 (1996).

36. Zheng, Q.S., Braunfeld, M.B., Sedat, J.W. & Agard, D.A. An improved strategy for automated electron microscopic tomography. *J. Struct. Biol.* **147**, 91–101 (2004).
37. Scheres, S.H.W., Melero, R., Valle, M. & Carazo, J.-M. Averaging of electron subtomograms and random conical tilt reconstructions through likelihood optimization. *Structure* **17**, 1563–1572 (2009).
38. Förster, F., Pruggnaller, S., Seybert, A. & Frangakis, A.S. Classification of cryo-electron sub-tomograms using constrained correlation. *J. Struct. Biol.* **161**, 276–286 (2008).
39. Sikorski, R.S. & Hieter, P. A system of shuttle vectors and yeast host strains designed for efficient manipulation of DNA in *Saccharomyces cerevisiae*. *Genetics* **122**, 19–27 (1989).
40. Ohi, M., Li, Y., Cheng, Y. & Walz, T. Negative staining and image classification - powerful tools in modern electron microscopy. *Biol. Proced. Online* **6**, 23–34 (2004).
41. Quispe, J. *et al.* An improved holey carbon film for cryo-electron microscopy. *Microsc. Microanal.* **13**, 365–371 (2007).
42. Mindell, J.A. & Grigorieff, N. Accurate determination of local defocus and specimen tilt in electron microscopy. *J. Struct. Biol.* **142**, 334–347 (2003).
43. Egelman, E.H. A robust algorithm for the reconstruction of helical filaments using single-particle methods. *Ultramicroscopy* **85**, 225–234 (2000).
44. Sachse, C. *et al.* High-resolution electron microscopy of helical specimens: a fresh look at tobacco mosaic virus. *J. Mol. Biol.* **371**, 812–835 (2007).
45. Frank, J. *Three-Dimensional Electron Microscopy of Macromolecular Assemblies* (Academic Press, San Diego, 1996).
46. Pettersen, E.F. *et al.* UCSF Chimera: a visualization system for exploratory research and analysis. *J. Comput. Chem.* **25**, 1605–1612 (2004).
47. Muller, E.G. A glutathione reductase mutant of yeast accumulates high levels of oxidized glutathione and requires thioredoxin for growth. *Mol. Biol. Cell* **7**, 1805–1813 (1996).
48. Muller, E.G. *et al.* The organization of the core proteins of the yeast spindle pole body. *Mol. Biol. Cell* **16**, 3341–3352 (2005).
49. Shimogawa, M.M., Widlund, P.O., Riffle, M., Ess, M. & Davis, T.N. Bir1 is required for the tension checkpoint. *Mol. Biol. Cell* **20**, 915–923 (2009).
50. Pei, J., Kim, B.H. & Grishin, N.V. PROMALS3D: a tool for multiple protein sequence and structure alignments. *Nucleic Acids Res.* **36**, 2295–2300 (2008).
51. Sali, A. & Blundell, T.L. Comparative protein modelling by satisfaction of spatial restraints. *J. Mol. Biol.* **234**, 779–815 (1993).
52. Trabuco, L.G., Villa, E., Mitra, K., Frank, J. & Schulten, K. Flexible fitting of atomic structures into electron microscopy maps using molecular dynamics. *Structure* **16**, 673–683 (2008).

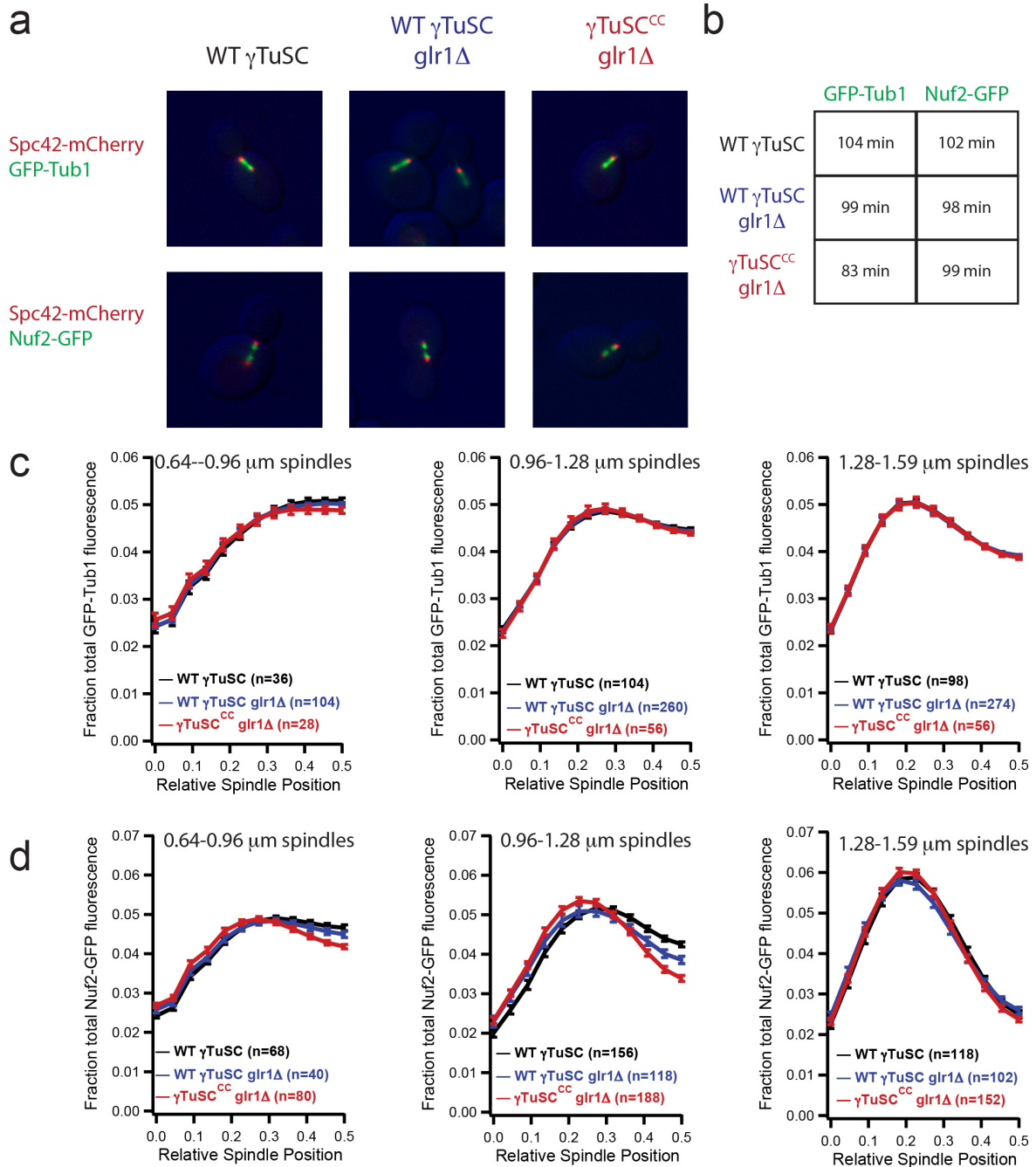




### Supplementary Figure 1

The structure of wild-type  $\gamma$ TuSC oligomers does not perfectly match 13-protofilament-microtubule geometry.

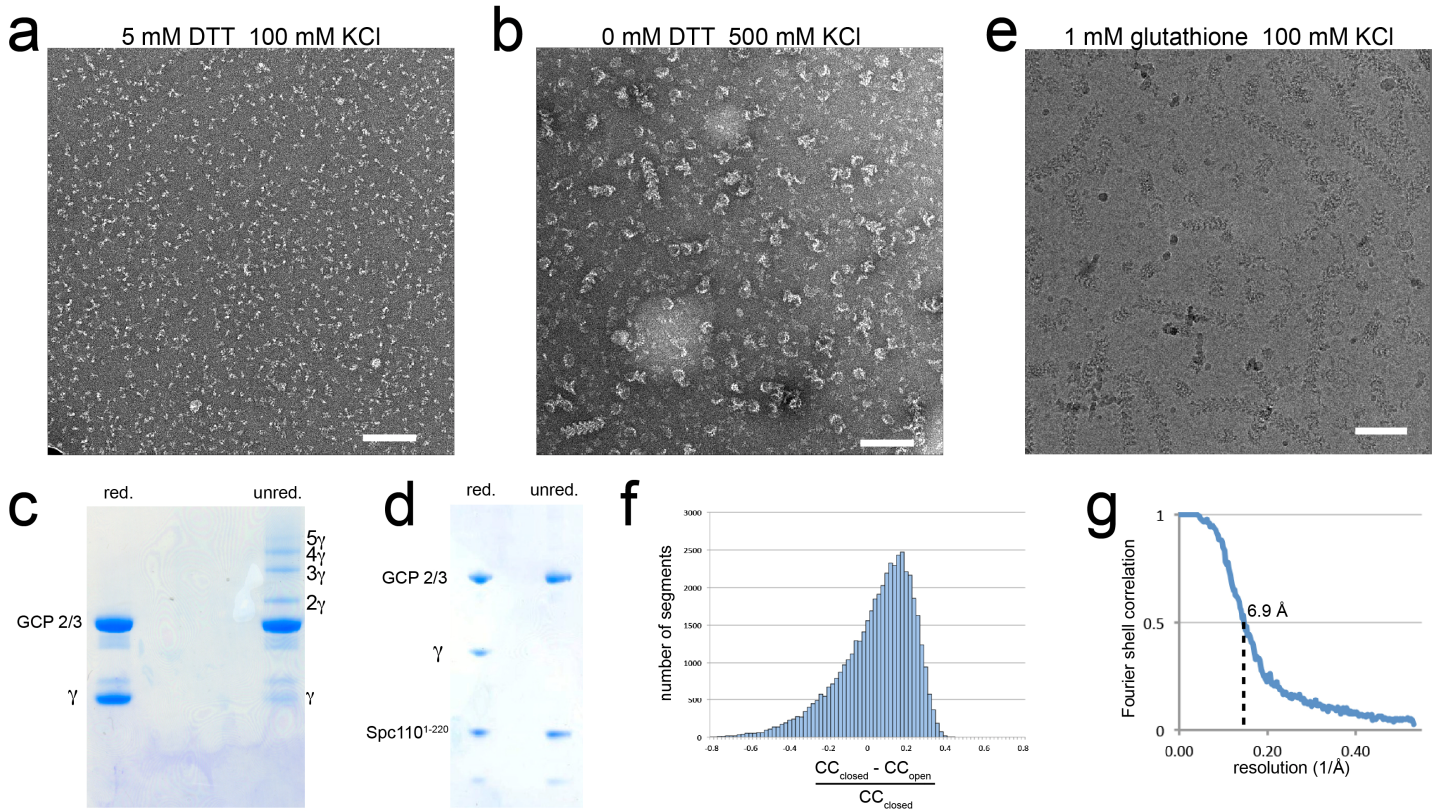
a) Two laterally-associated  $\gamma$ TuSC subunits from ring-like  $\gamma$ TuSC assemblies are shown. The two  $\gamma$ -tubulins (gold) within each  $\gamma$ TuSC are held separate from each other by GCP2 and GCP3, while the  $\gamma$ -tubulins at the inter- $\gamma$ TuSC interface are positioned with microtubule-like lateral contacts. b) The intra- $\gamma$ TuSC separation results in a staggered pattern of  $\gamma$ -tubulin in  $\gamma$ TuSC assemblies, with a helical pitch of 147 Å. c) By contrast, lateral contacts between tubulin subunits in a microtubule are uniform around the filament, and have a helical pitch of 122 Å. d) To illustrate the mismatch between  $\gamma$ TuSC oligomers and the microtubule, the upper  $\gamma$ -tubulin in the ring has been aligned to make longitudinal contacts with  $\alpha$ -tubulin at the minus end of the microtubule. This would result in a large gap between  $\alpha$ - and  $\gamma$ -tubulin at the last position in the ring.



## Supplementary Figure 2

$\gamma$ TuSC<sup>CC</sup> does not affect cell viability.

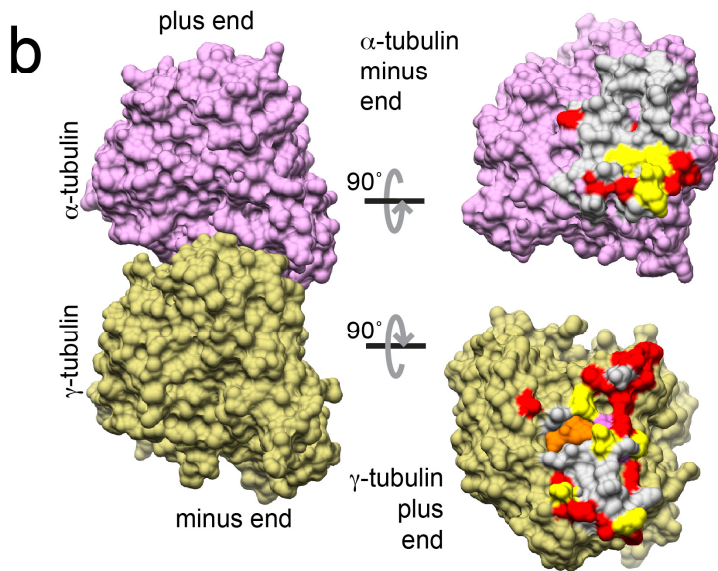
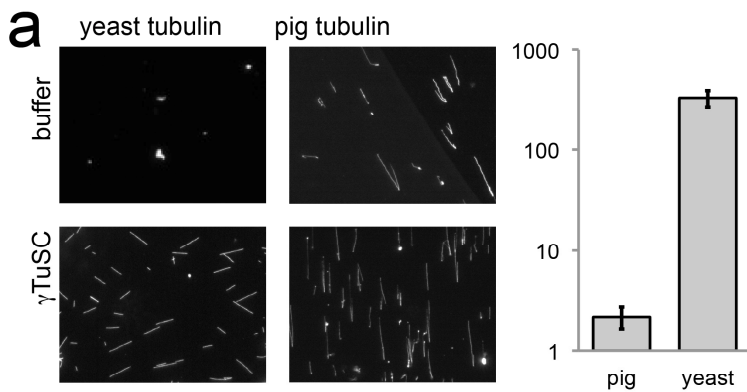
a) Representative images of WT, *glr1* $\Delta$ , and  $\gamma$ TuSC<sup>CC</sup> *glr1* $\Delta$  fluorescent strains. GLR1 encodes glutathione reductase; *glr1* $\Delta$  cells were used to maximize the chance that the  $\gamma$ TuSC<sup>CC</sup> disulfides would be oxidized. Cells in the top row have the spindle pole bodies marked by Spc42-mCherry and the microtubules marked by GFP-Tub1. Cells in the bottom row have the spindle pole bodies marked by Spc42-mCherry and the kinetochores marked by Nuf2-GFP. b) The doubling times of WT and  $\gamma$ TuSC<sup>CC</sup> strains. c) Average GFP-Tub1 fluorescence distributions show that  $\gamma$ TuSC<sup>CC</sup> has no effect on tubulin distribution across three spindle length classifications. d) Average Nuf2-GFP fluorescence distributions show that  $\gamma$ TuSC<sup>CC</sup> has no effect on kinetochore clustering in metaphase spindles (1.28-1.59  $\mu$ m), while shorter spindles show kinetochores cluster slightly closer to the spindle pole bodies. Error bars represent the standard error of the mean.



**Supplementary Figure 3**

Cross-linking and structural analysis of  $\gamma$ TuSC<sup>CC</sup>.

a)  $\gamma$ TuSC<sup>CC</sup> in the presence of 5 mM DTT is predominantly monomeric complex, although  $\gamma$ TuSC pairs were frequently observed. b) Under non-reducing conditions  $\gamma$ TuSCs spontaneously assemble into oligomers, even in the presence of 500 mM KCl, which prevents association of wildtype  $\gamma$ TuSC. c) SDS-PAGE of  $\gamma$ TuSC<sup>CC</sup> under reducing conditions (5 mM DTT), and non-reducing conditions (0 mM DTT). In the non-reducing condition  $\gamma$ -tubulin forms disulfide crosslinks, resulting in a ladder of 1-5  $\gamma$ -tubulin chains. Formation of  $\gamma$ -tubulin oligomers greater than two chains indicates that crosslinks were formed at both inter- $\gamma$ TuSC and intra- $\gamma$ TuSC interfaces. d) Co-purified  $\gamma$ TuSC<sup>CC</sup> and Spc110<sub>1-220</sub> was dialyzed for 72 h. against an oxidizing buffer containing 1mM oxidized glutathione. On SDS-PAGE the reduced sample has the expected bands for Spc110<sub>1-220</sub>,  $\gamma$ -tubulin, and GCP2/GCP3, while in the unreduced sample extensive  $\gamma$ -tubulin crosslinking prevents its migration into the gel. This highly-cross-linked sample was used for cryo-EM imaging. e) Cryo-EM image of cross-linked  $\gamma$ TuSC<sup>CC</sup>-Spc110<sub>1-220</sub> filaments (same sample as in d). f) Segments of  $\gamma$ TuSC<sup>CC</sup> filaments were compared to projections of the  $\gamma$ TuSC filament in the open state and a preliminary reconstruction of the closed state. The histogram plots the fractional difference in correlation coefficient, with negative values representing a better match to the open state. Segments matching better to the open state were omitted from the final refinement of the closed filament structure. g) Fourier shell correlation (FSC) of the final  $\gamma$ TuSC<sup>CC</sup>-Spc110<sub>1-220</sub> reconstruction indicates a resolution of 6.9 Å at the 0.5 cutoff. Scalebars, 100 nm.



**c**

yeast $\alpha$	MREVISINVQAGCQIGNACWELYSLEHGIKPDGHLEDGLSKPKGGEGEF 50
pig $\alpha$	MREVISIHVGGAGVQIGNACWELYSLEHGIQPDGQMPSPDR-TTGGGDSGF 49
yeast $\alpha$	STFFHETGYGKFPVRAIYVDLEPNVIDEVRNGPYKDLFHPQLISGKEDA 100
pig $\alpha$	NTFFSETGAGKHVPRAVFDLEPTVIDEVRTGTYRQLFHPQLITGKEDA 99
yeast $\alpha$	ANNYARGHYTVGREILGDVLDLRIRKLDQCDGLQGFTHSLGGGTSGSL 150
pig $\alpha$	ANNYARGHYTIKGEIIDLVDLRIRKLDQCTGLQGFVPHSPGGGTSGSF 149
yeast $\alpha$	GSLLEELSAEYGGKSKLEFAVYAPQVSTSVVEPYNTVLTHTTLEHSD 200
pig $\alpha$	TSLLMERLSVDYGGKSKLEFSIYAPQVSTAVVEPYNSILTHTTLEHSD 199
yeast $\alpha$	CTFMVDNEAIYDMCKRNLDIRPSPANLNLIQVVS SVTASLRFDGSLN 250
pig $\alpha$	CAPMVDNEAIYDICRNRLLDIERPTTYNLNRLIGQIVSSITASLRFDGALN 249
yeast $\alpha$	VDLNEFQTNLVPPYPRHIFPLVSVSPVLSKSKS---ESNSVSEITNACFEFG 296
pig $\alpha$	VDLTEFQTNLVPPYPRGHFFLATYAPVISAEKAYHEQLSVAEITNACFEPA 299
yeast $\alpha$	NQMVKCDPRDGKYMATCLLYRGGDVVT DVVRAEQVKNKKT VQLVDCWCT 346
pig $\alpha$	NQMVKCDPRHGKYMATCLLYRGGDVVP DVVAAATIKKRTIQFVDCWCT 349
yeast $\alpha$	GFKGICYEPTTAPNSQLATVDRVAVCMLSNNTSIAEAWKRIDRRFDLMY 396
pig $\alpha$	GFKGINYEPTTVPVGGDLAKVQRAVAVCMLSNNTSIAEAWRLDHRFDLMY 399
yeast $\alpha$	AKRAFVHWYVGEEMEGEFTPEAREDLAALERDYIEVGAD- 435
pig $\alpha$	AKRAFVHWYVGEEMEGEFTPEAREDMAALEKDYEEVGVDS 439

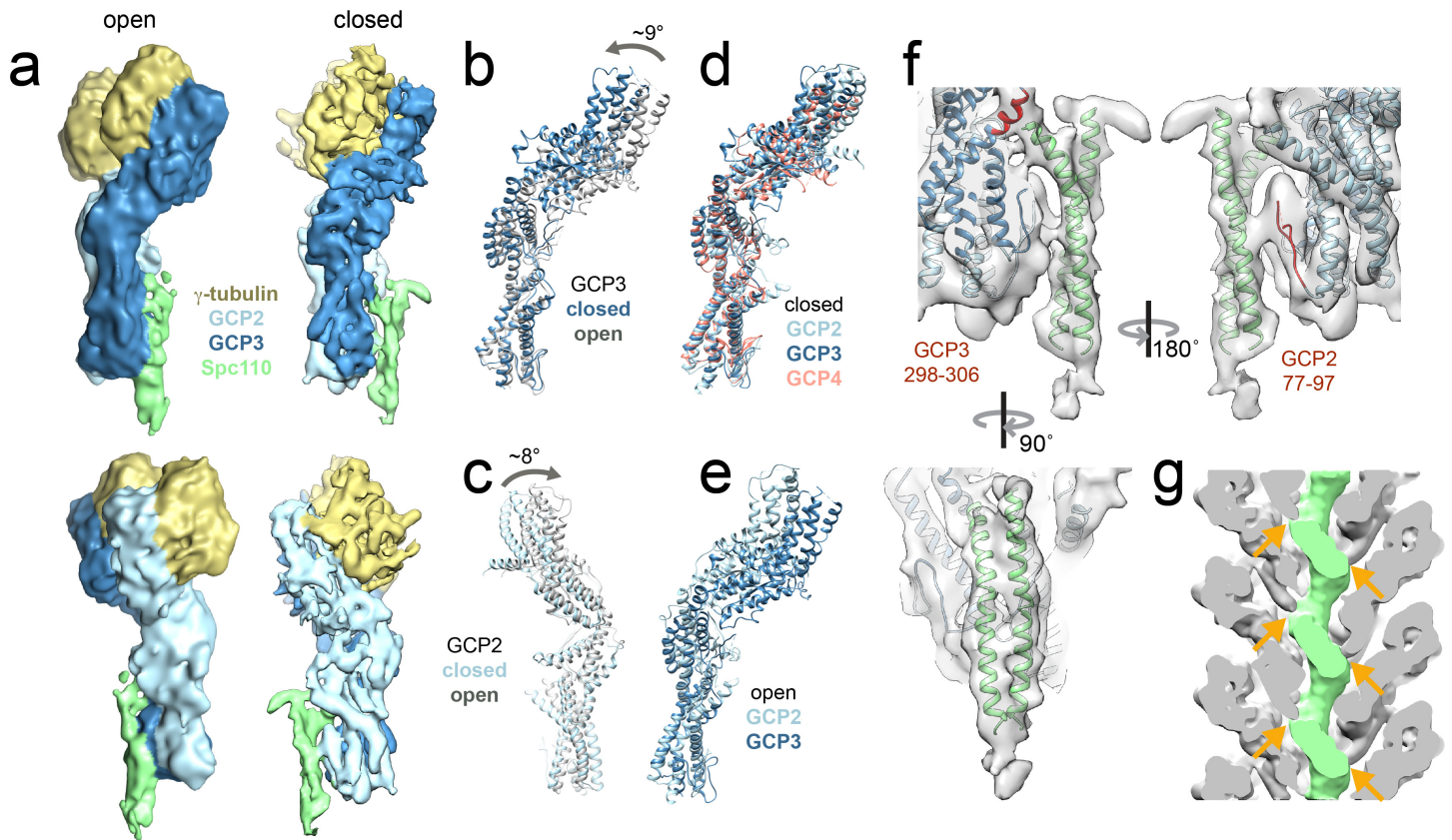
**d**

yeast $\gamma$	MGGEIITLQAGCGNHVGFWSQLAKEHAIGTDGLSQLPDSSTERDDDT 50
human $\gamma$	--REIITLQLGCGNQIGFEPFKQLCAEHGISPEAIVE--EFATEGTRDK 46
yeast $\gamma$	KPFFRENSRNKFTPRAIMDSEPVVIADVE-NTRFGFPDPRNTWVASDGA 99
human $\gamma$	DVFFYQADDEHYIPRAVLLDLEPRVIHSILNSPKALYNPENIYLSEHG- 95
yeast $\gamma$	SAGNSWANGYDIGTRNQDDILNLIKDEIDSTDNFEGFQLLHVSAGGTGSG 149
human $\gamma$	--AGNNWASGFSQGEKIHEDIFDIIDREADGSDSLGFLVCHSIAAGTGTSG 144
yeast $\gamma$	LGSNLEALCDRYPKKILTTYSVFPAS--S VVVSQYNTILALRRLIED 197
human $\gamma$	LGSYLLERLNDRYPKKLVQTYSVFPNDPMS VVVSQYNSLLTLKRLTQN 194
yeast $\gamma$	SDATVVPDNASLLNISGKVFRRNPIDQHTNQLISTIISSVTNSIRFSPY 247
human $\gamma$	ADCLVVDLNTALNRIATDRLHIQNPSSQINQLVSTIMSASTTLRLPYGY 244
yeast $\gamma$	MYSSMSIYSTLIPSELHFLSPSFTPFTHS-SYDVMLDLLDPSNSLVST 296
human $\gamma$	MNNDLIGLIASLIPTPRHLFMTGYTPTLTKTTVLDVMRRLQPKNVVST 294
yeast $\gamma$	AMNNPTYFNVYNTIIGNVEPRQISRAMTKLQRI-KPSSWSSSAMHVNIG 345
human $\gamma$	--TNHCYIATILNIQGEVDPTQVHKSLQRIRERLANFIPWGPASIQVALS 342
yeast $\gamma$	RR----SVSGMMLSNMSTVVVFNACNTPDKFAAGAPLNINNVGDLF 390
human $\gamma$	RKSPYLPRVSGLMMANHTSISLFFERTCRQYDKRKREAFLEFRKEDMF 392
yeast $\gamma$	QSMQNVQDEFAESREVQSLMEDYVAAEQDSYL-- 423
human $\gamma$	KDN---FDEMDTSREIVQQLDEYHAATRPDIISW 424

## Supplementary Figure 4

Yeast  $\gamma$ TuSC nucleation activity is species specific.

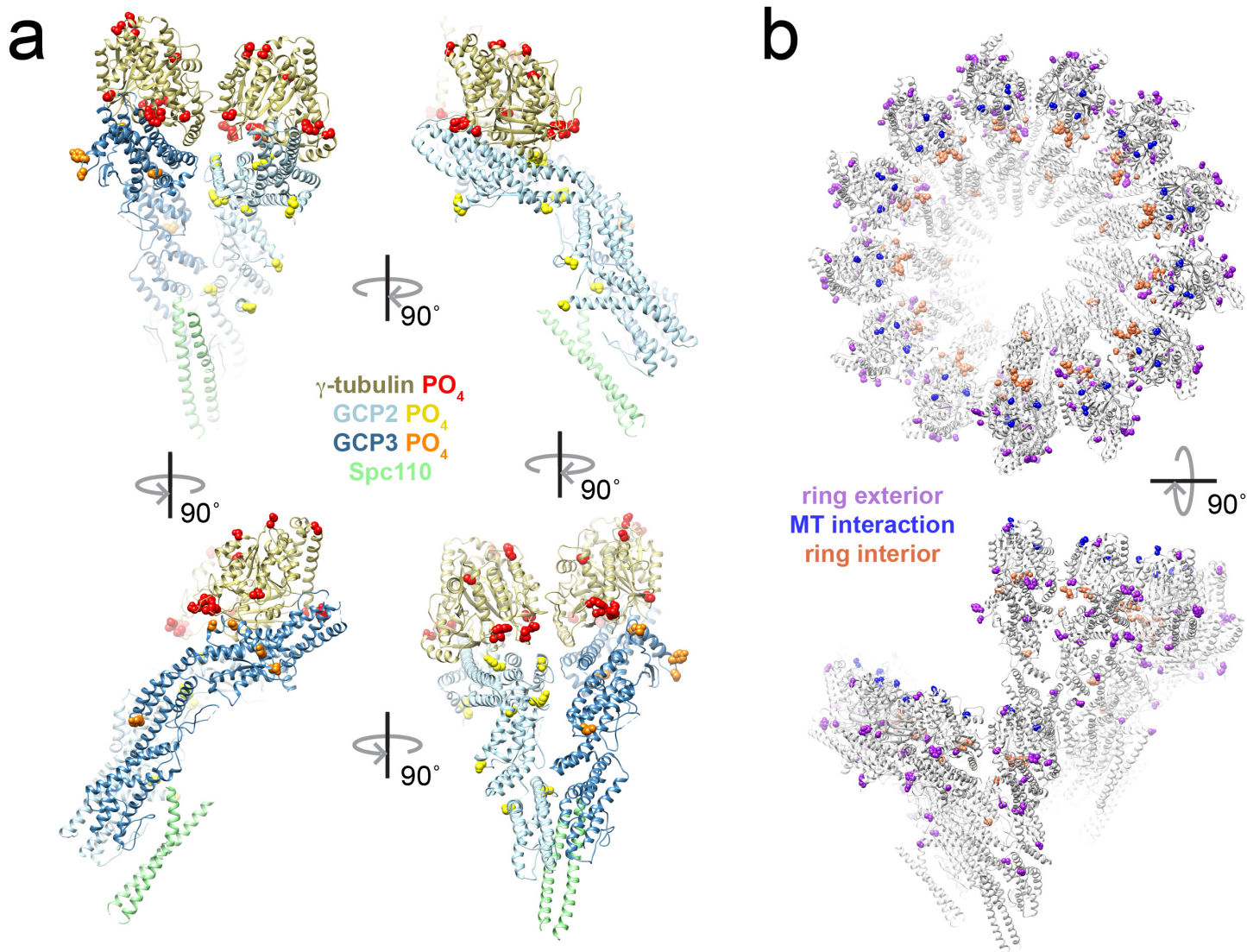
a) Comparison of nucleating activity of  $\gamma$ TuSC rings with yeast and pig brain tubulin. Nucleation assays were performed as in Fig. 3C (data for yeast tubulin is the same as Fig. 3C), except that the experiments with brain tubulin were at 12  $\mu$ M tubulin and 37 $^{\circ}$  C (n=4 independent experiments; error bars represent the s.e.m.). b) The predicted longitudinal interaction between  $\alpha$ - and  $\gamma$ -tubulin is shown at left. Human  $\gamma$ -tubulin and pig  $\alpha$ -tubulin are shown as these are the existing crystal structures. At right the interaction surfaces are highlighted as a function of the conservation between yeast and vertebrate tubulin: grey sites are identical, yellow have conservative amino acid substitutions, red have non-conservative substitutions, magenta is a two amino acid insertion in  $\gamma$ -tubulin, and GTP is shown in orange. c) Binary sequence alignment of yeast and vertebrate  $\alpha$ -tubulin. d) Binary sequence alignment of yeast and vertebrate  $\gamma$ -tubulin. Color in g (c) and (d) is the same as for (b).



### Supplementary Figure 5

Subunit localization and conformation in the  $\gamma$ TuSC closed-state structure.

Comparison of the open and closed states of  $\gamma$ TuSC. The elongated GCP2 and GCP3 structures each appear slightly straightened. b) Overlay of GCP3 in the open (grey) and closed (blue) states shows that it straightens by about  $9^\circ$ . c) Overlay of GCP2 in the open (grey) and closed (blue) states shows that it straightens by about  $8^\circ$ . d) Superposition of GCP2 and GCP3 in the closed state shows that they are in very similar overall conformation. GCP4, which was used as the starting structure for homology modeling both GCP2 and GCP3, is in a similar overall conformation. e) Superposition of GCP2 and GCP3 in the open state. For B-E all structural alignments were done using the two N-terminal helical bundles. f) The density predicted to correspond to part of Spc110<sub>1-220</sub> resembles a two-stranded coiled-coil. A generic two-stranded coiled coil was used to model Spc110, and flexibly fit into the EM density. The closest contacts with Spc110 are between residues 77-97 of GCP2 (which includes 9 residues not included in our model) near the very base of  $\gamma$ TuSC, and further up the structure with residues 119-126 of GCP3. g) A cutaway view of the  $\gamma$ TuSC<sup>CC</sup> filament in the closed state, low-pass filtered at 15 Å. The  $\gamma$ TuSC and modeled Spc110 structure is colored grey, and disordered density that runs along the center of the filament is colored green. Arrows denote the connections between the ends of the modeled Spc110 structure and the disordered density, which suggest that the disordered density is composed of flexible regions of Spc110<sub>1-220</sub>.



**Supplementary Figure 6**

Mapping phosphorylation sites on the  $\gamma$ TuSC structure.

a) A single  $\gamma$ TuSC is shown with residues known to be phosphorylated highlighted as spheres in red, yellow, and orange for sites on  $\gamma$ -tubulin, GCP2, and GCP3 respectively. c) The model of yeast  $\gamma$ TuRC with known phosphorylation sites rendered as spheres. Sites freely accessible on the outer surface of the ring are colored purple, sites at the plus end of  $\gamma$ -tubulin predicted to be involved in longitudinal contacts with the microtubule in blue, and sites on the ring interior that would be inaccessible when a microtubule is bound are coral.